Supporting Information

Direct Electrosynthesis of Ammonia from Nitrate Reduction Using Atomically Precise Carbonyl-Rich Metal Clusters in Neutral Media

Authors:

Miao Wang,[1,2,#] Tianyu Shen,[1,#] Heng Zhou,[3,#] Shuaikang Yang,[1] Fengkun Hao,[2] Chaohui Wang,[2] Mohan Kumar,[4] Zuoxiu Tie,[1,*] Shuangming Chen,[3,*] Zhanxi Fan,[2,*] and Zhong Jin[1,*]

Affiliations:

[1] State Key Laboratory of Coordination Chemistry, MOE Key Laboratory of Mesoscopic Chemistry, MOE Key Laboratory of High Performance Polymer Materials and Technology, Jiangsu Key Laboratory of Green Energy Catalysis and Intelligent Chemical Engineering, Suzhou Key Laboratory of Green Intelligent Manufacturing of New Energy Materials and Devices, Tianchang New Materials and Energy Technologies Research Center, Institute of Green Chemistry and Engineering, School of Chemistry and Chemical Engineering, Nanjing University, Nanjing, Jiangsu 210023, P. R. China.

[2] Department of Chemistry, Hong Kong Branch of National Precious Metals Material Engineering Research Center (NPMM), Hong Kong Institute for Clean Energy, City University of Hong Kong, Kowloon, Hong Kong, 999077, P. R. China.

[3] National Synchrotron Radiation Laboratory, Chinese Academy of Sciences Center for Excellence in Nanoscience, University of Science and Technology of China, Hefei, Anhui 230029, P. R. China.

[4] Department of Chemistry, PES Institute of Technology and Management, Shivamogga, Karnataka 577204, India.

# These authors contributed equally to this work.

* Email addresses of corresponding authors: zxtie@nju.edu.cn; csmp@ustc.edu.cn; zhanxi.fan@cityu.edu.hk; zhongjin@nju.edu.cn

This file includes:

Experimental section

Density functional theory (DFT) computation details

Figure S1–S22

Table S1–S2

Experimental section

Chemicals and materials

All the carbonyl-rich metal clusters investigated in this study were received from Shanghai Aladdin Biochemical Technology Co., Ltd.. Co_2-CRMC [Dicobalt octacarbonyl ($Co_2(CO)_8$, 98%)], Co_4-CRMC [Tetracobalt dodecacarbonyl ($Co_4(CO)_{12}$, 98%)], Ru_3-CRMC [Triruthenium dodecacarbonyl ($Ru_3(CO)_{12}$, 99%)], Fe_2-CRMC [Diiron nonacarbonyl ($Fe_2(CO)_9$, 97%)], Fe_3-CRMC [Triiron dodecacarbonyl ($Fe_3(CO)_{12}$, 96%)], Mn_2-CRMC [Dimanganese decacarbonyl ($Mn_2(CO)_{10}$, 98%)], Mo-CRMC [Molybdenum hexacarbonyl ($Mo(CO)_6$, 98%)], and W-CRMC [Tungsten hexacarbonyl ($W(CO)_6$, 97%)].

Material characterizations

The crystalline structures and phase compositions of the samples were analyzed using powder X-ray diffraction (PXRD, Bruker D8 Advance diffractometer) with a Cu Ka (λ = 1.5418 Å) radiation source. Attenuated total reflectance Fourier transform infrared (ATR-FTIR) spectra were measured on a Thermo Fisher Scientific Optics NICOLETIS10 FTIR spectrometer with a Universal ATR accessory in the range of 4000 to 400 cm^{-1}. Field-emission scanning electron microscopy (FE-SEM, FEI Nova Nano-450 instrument) was utilized for morphological and structural characterizations. Transmission electron microscopy (TEM) was conducted using a JEM-2100 instrument. To investigate the detailed surface compositions and valence states of all samples, X-ray photoelectron spectroscopy (XPS) was carried out using a PHI-5000 Versa Probe instrument. The K-edge extended X-ray absorption fine structure spectroscopy (EXAFS) was conducted by the transition mode at the BL14W1 end station in the Shanghai Synchrotron Radiation Facility (SSRF). The acquired EXAFS

data were processed and fitted according to standard procedures using the ATHENA module of the IFEFFIT software packages. The UV-Vis absorbance data were measured using a Shimadzu UV-2600 spectrophotometer.

Electrocatalytic nitrate reduction reaction (NITRR) measurements

For the preparation of working electrodes, a piece of carbon paper (CP, 1 × 1 cm^2) was cleaned using acetone, alcohol, and water, then dried in a vacuum oven at 80 ºC. The electrocatalyst ink was created by dispersing 4 mg of the specific sample in a 1:1 mixture of deionized (DI) water and ethanol (900 μL), followed by the addition of 100 μL Nafion. This mixture was ultrasonicated for 30 minutes. Afterward, 100 μL of the electrocatalyst ink was applied to the CP and dried at room temperature. The NITRR measurements were conducted with a CHI-760E electrochemical workstation at room temperature and ambient pressure using an H-type cell divided by a Nafion-117 proton exchange membrane. A platinum disk electrode (1 × 1 cm^2) served as the counter electrode, while a saturated Ag/AgCl electrode served as the reference electrode. For industrially relevant current density performances in NITRR, the custom-made flow cell was employed. The electrolyte was purged with high-purity Ar gas flow for 5 min prior to the NITRR measurements. Linear sweep voltammetry (LSV) tests were conducted at a scan rate of 5 mV/s. After each electrolysis operation, the electrolyte was analyzed using UV-Vis absorption spectrophotometry, as described below. All applied potentials were calibrated against the reversible hydrogen electrode (RHE) using the following equation:

$$E\ (vs.\ RHE) = E\ (vs.\ Ag/AgCl) + 0.1989 + 0.059 \times pH \qquad \text{(Equation 1)}$$

Determination of ammonia concentrations

The ammonia concentrations were determined using the standard indophenol blue method. A mixture was prepared by combining 2.0 mL of the post-electrolysis electrolyte with 2.0 mL of a 1.0 M NaOH solution containing 5% salicylic acid and 5% sodium citrate, 1.0 mL of 50 mM NaClO, and 0.2 mL of a 1% sodium nitroferricyanide (III) dihydrate solution ($C_5FeN_6Na_2O \cdot 2H_2O$). After standing in darkness for 2 h, the mixture was analyzed using a UV-Vis spectrophotometer (UV-2600, Shimadzu) to obtain the absorption spectra. The peak value at λ = 655 nm in the indophenol blue spectrum was compared to a standard curve to quantify the NH_3 produced.

Determination of NO_2^-

To quantify nitrite (NO_2^-) levels, we employed a colorimetric Griess assay. The Griess reagent was formulated by combining 0.1 g of N-(1-naphthyl)ethylenediamine dihydrochloride, 1.0 g of sulfanilamide, and 2.9 mL of phosphoric acid (H_3PO_4) in 50 mL of deionized water. For the analysis, 1 mL of the nitrite-containing sample was added to 1 mL of the prepared Griess reagent and diluted with 2 mL of deionized water. After thorough mixing, the solution was incubated at ambient temperature for 10 minutes. During incubation, sulfanilamide initially diazotizes with nitrite to form a diazonium intermediate, which then couples with N-(1-naphthyl)ethylenediamine to generate a stable magenta-colored azo compound. The absorbance of this colored product was recorded at 540 nm using a UV-Vis spectrophotometer. Finally, the concentration of nitrite was derived from the measured absorbance value by reference to a pre-established calibration curve.

Isotope labeling experiments

To investigate the source of the ammonia generated, ^{15}N isotopic tracer experiments were performed with $Na^{15}NO_3$ (98.3% enriched, Sigma) as the nitrogen precursor. The electrocatalytic NITRR test was carried out at −1.0 V (*vs*. RHE) in a 0.1 M Na_2SO_4 electrolyte containing 0.1 M $Na^{15}NO_3$. Following the reaction, 0.6 mL of the product solution was acidified with 0.1 mL of 1 M H_2SO_4. For ^1H NMR analysis, a glass capillary filled with D_2O was inserted into the sample. One-dimensional ^1H NMR spectra were then acquired using a Bruker Avance-600 superconducting Fourier transform NMR spectrometer.

Calculations of ammonia yield rates and Faradaic efficiencies

The ammonia yield rate was calculated via the following equation:

$$NH_3 \text{ yield rate } (mmol \cdot h^{-1} g^{-1}_{cat.}) = (C_{NH3} \times V)/(t \times m_{cat.}) \quad \text{(Equation 2)}$$

where C_{NH3} ($mmol \cdot mL^{-1}$) is the measured NH_3 concentration, V (mL) is the volume of the electrolyte, t (h) is the reaction time, and m (g) is the loading weight of the electrocatalyst on the CP.

The ammonia production Faradaic efficiency (FE_{NH3}) was calculated via the following equation:

$$FE_{NH3} = (n \times F \times C_{NH3} \times V)/(17 \times Q) \quad \text{(Equation 3)}$$

where n is the number of transferred electrons, C_{NH3} ($g \cdot mL^{-1}$) is the measured NH_3 concentration, F is the Faraday constant (96485 C mol^{-1}), and Q (C) is the total quantity of applied electricity.

***In situ* DEMS test**

In situ differential electrochemical mass spectrometry (DEMS) measurements were performed using a Linglu DEMS setup. The experiments employed a custom-built electrochemical cell, where the working, counter, and reference electrodes consisted of catalyst-loaded carbon paper, a Pt wire,

and a Hg/HgO electrode, respectively. A polytetrafluoroethylene (PTFE) membrane was utilized to isolate the gas and electrolyte. During measurement, the working electrode potential was linearly scanned from 0.2 to −1.0 V (*vs.* RHE) at a rate of 5 mV s^{-1} in an Ar-saturated 0.1 M Na_2SO_4 solution containing 0.1 M KNO_3, while the corresponding mass signals were continuously recorded.

In situ ATR-FTIR test

In situ attenuated total reflection–Fourier transform infrared (ATR-FTIR) spectroscopy was carried out using a Nicolet iS50 IR spectrometer equipped with a liquid-nitrogen-cooled mercury-cadmium-telluride (MCT) detector. The working electrode was an Au-coated silicon hemispherical prism (20 mm diameter, MTI Corporation) modified with the electrocatalyst. Infrared spectra were recorded in absorption mode at a resolution of 8 cm^{-1}, accumulating 32 scans per spectrum. During measurement, a linear sweep voltammetry (LSV) profile was obtained by scanning the potential from 0.2 to –0.8 V (*vs.* RHE) at 5 mV s^{-1}. All collected spectra were background-subtracted for further analysis.

Density functional theory (DFT) computation details

All theoretical calculations were performed using Materials Studio. Geometric optimizations and electronic property calculations were meticulously conducted using the CASTEP module. The electronic exchange and correlation energies were accurately depicted by employing the Perdew-Burke-Ernzerhof (PBE) functional within the framework of Generalized Gradient Approximation (GGA), ensuring precision in the computational models.[S1] The van der Waals interaction was taken into consideration by the Grimme method, and the kinetic energy cutoff was chosen to be set as 570

eV.[S2,S3] In order to save computational cost, a simplified Co_2-CRMC cluster structure was then built to simulate Co_2-CRMC model with 72 atoms in a unit cell. A periodic boundary condition (PBC) model with the cell size of 10 × 10 × 20 $Å^3$ was employed to model the Co_2-CRMC system. The Brillouin zone was sampled by a k-point mesh of 1 × 1 × 1. The energy convergence value between two consecutive steps was chosen as 1 × 10^{-5} eV/atom, a maximum force was allowed lower than 0.03 eV/Å, and a maximum displacement was allowed lower than 0.001 Å.

In order to describe the charged NO_3^- species in the periodic DFT calculations, gaseous HNO_3 was chosen as a reference based on the following steps:[S4,S5]

$$HNO_3\ (g) \rightarrow HNO_3\ (l) \quad (1)$$

$$HNO_3\ (l) \rightarrow H^+ + NO_3^- \quad (2)$$

$$* + NO_3^- \rightarrow *NO_3 + e^- \quad (3)$$

The adsorption free energy of NO_3^- (ΔG_{*NO3}) can be obtained by the following calculation:

$$\Delta G_{*NO3} = G_{*NO3} - G_{*} - G_{HNO3(g)} + 1/2G_{H2(g)} + \Delta G_{correct} \quad (4)$$

where G_{*NO3}, G_{*}, $G_{HNO3(g)}$, and $G_{H2(g)}$ are the Gibbs free energy of NO_3^- adsorbed on Co_2-CRMC, Co_2-CRMC, HNO_3, and H_2 molecules, respectively. $\Delta G_{correct}$ is the correction of adsorption energy of NO_3^- species, in which $\Delta G_{correct}$ is 0.392 eV according to CRC handbook of chemistry and physics.[S6]

The NITRR process experiences the transfer of nine protons and eight electrons. The possible pathways of NO_3^- reduction can be classified as N-end and O-end pathways, according to different adsorption configurations of NO intermediate as demarcation. The elementary steps of N-end pathway can be described as follows

$$HNO_3 + * \rightarrow *NO_3 + H^+ + e^- \quad (5)$$

$$*NO_3 + H^+ + e^- \rightarrow *HNO_3 \quad (6)$$

$$*HNO_3 + H^+ + e^- \rightarrow *NO_2 + H_2O \quad (7)$$

$$*NO_2 + H^+ + e^- \rightarrow *HNO_2 \quad (8)$$

$$*HNO_2 + H^+ + e^- \rightarrow *NO + H_2O \quad (9)$$

$$*NO + H^+ + e^- \rightarrow *NOH \quad (10)$$

$$*NOH + H^+ + e^- \rightarrow *N + H_2O \quad (11)$$

$$*N + H^+ + e^- \rightarrow *NH \quad (12)$$

$$*NH + H^+ + e^- \rightarrow *NH_2 \quad (13)$$

$$*NH_2 + H^+ + e^- \rightarrow *NH_3 \quad (14)$$

If the *ON is formed, the O-end pathway can be expressed as:

$$*HNO_2 + H^+ + e^- \rightarrow *ON + H_2O \quad (15)$$

$$*ON + H^+ + e^- \rightarrow *ONH \quad (16)$$

$$*ONH + H^+ + e^- \rightarrow *ONH_2 \quad (17)$$

$$*ONH_2 + H^+ + e^- \rightarrow *O + NH_3 \quad (18)$$

$$*O + H^+ + e^- \rightarrow *OH \quad (19)$$

$$*OH + H^+ + e^- \rightarrow *H_2O \quad (20)$$

The Gibbs free energy changes along the pathway can be obtained by the following equations:

$$\Delta G_{*HNO3} = G_{*HNO3} - G_{*NO3} - 1/2G_{H2} \quad (21)$$

$$\Delta G_{*NO2} = G_{*NO2} - G_{*NO3} + G_{H2O} - G_{H2} \quad (22)$$

$$\Delta G_{*HNO2} = G_{*HNO2} - G_{*NO3} + G_{H2O} - 3/2G_{H2} \quad (23)$$

$$\Delta G_{*NO} = G_{*NO} - G_{*NO3} + 2G_{H2O} - 2G_{H2} \quad (24)$$

$$\Delta G_{*NOH} = G_{*NOH} - G_{*NO3} + 2G_{H2O} - 5/2G_{H2} \quad (25)$$

$$\Delta G_{*N} = G_{*N} - G_{*NO3} + 3G_{H2O} - 3G_{H2} \quad (26)$$

$$\Delta G_{*NH} = G_{*NH} - G_{*NO3} + 3G_{H2O} - 7/2G_{H2} \quad (27)$$

$$\Delta G_{*NH2} = G_{*NH2} - G_{*NO3} + 3G_{H2O} - 4G_{H2} \quad (28)$$

$$\Delta G_{*NH3} = G_{*NH3} - G_{*NO3} + 3G_{H2O} - 9/2G_{H2} \quad (29)$$

$$\Delta G_{*ON} = G_{*ON} - G_{*NO3} + 2G_{H2O} - 2G_{H2} \quad (30)$$

$$\Delta G_{*ONH} = G_{*ONH} - G_{*NO3} + 2G_{H2O} - 5/2G_{H2} \quad (31)$$

$$\Delta G_{*ONH2} = G_{*ONH2} - G_{*NO3} + 2G_{H2O} - 3G_{H2} \quad (32)$$

$$\Delta G_{*O} = G_{*O} - G_{*NO3} + 2G_{H2O} + G_{NH3} - 7/2G_{H2} \quad (33)$$

$$\Delta G_{*OH} = G_{*OH} - G_{*NO3} + 2G_{H2O} + G_{NH3} - 4G_{H2} \quad (34)$$

$$\Delta G_{*H2O} = G_{*H2O} - G_{*NO3} + 2G_{H2O} + G_{NH3} - 9/2G_{H2} \quad (35)$$

where G_{*NO3}, G_{*HNO3}, G_{*NO2}, G_{*HNO2}, G_{*NO}, G_{*NOH}, G_{*N}, G_{*NH}, G_{*NH2}, and G_{*NH3} are the free energies of the $*NO_3$, $*HNO_3$, $*NO_2$, $*HNO_2$, *NO, *NOH, *N, *NH, $*NH_2$ and $*NH_3$ intermediates adsorbed at the Co site along the N-end pathway, respectively. While G_{*ON}, G_{*ONH}, G_{*ONH2}, G_{*O}, G_{*OH}, and G_{*H2O} referred to the free energies of the *ON, *ONH, $*ONH_2$, *O, *OH, and $*H_2O$ species during the O-end pathway, respectively. The free energies of gaseous NH_3, H_2O, and H_2 molecules can be denoted as G_{NH3}, G_{H2O}, and G_{H2}, respectively. The values for the free energies of each gaseous and adsorbed species are calculated by:

$$G = E_{total} + E_{ZPE} - TS \quad (36)$$

where E_{total} is the total energy from the DFT calculations, E_{ZPE} is the zero-point energy, S is the entropy, and T is the temperature. It should be mentioned that the established computational hydrogen electrode (CHE) model was applied to investigate the electrochemical processes. The theoretical basis for the CHE model is that electrochemical reactions occurred in the solution normally with small kinetic barriers, which are surmountable at room temperature. The reaction

kinetics will be dependent on the free energy difference of each step. The step with the most positive free energy difference could be the rate-determining step possibly[S4–S6].

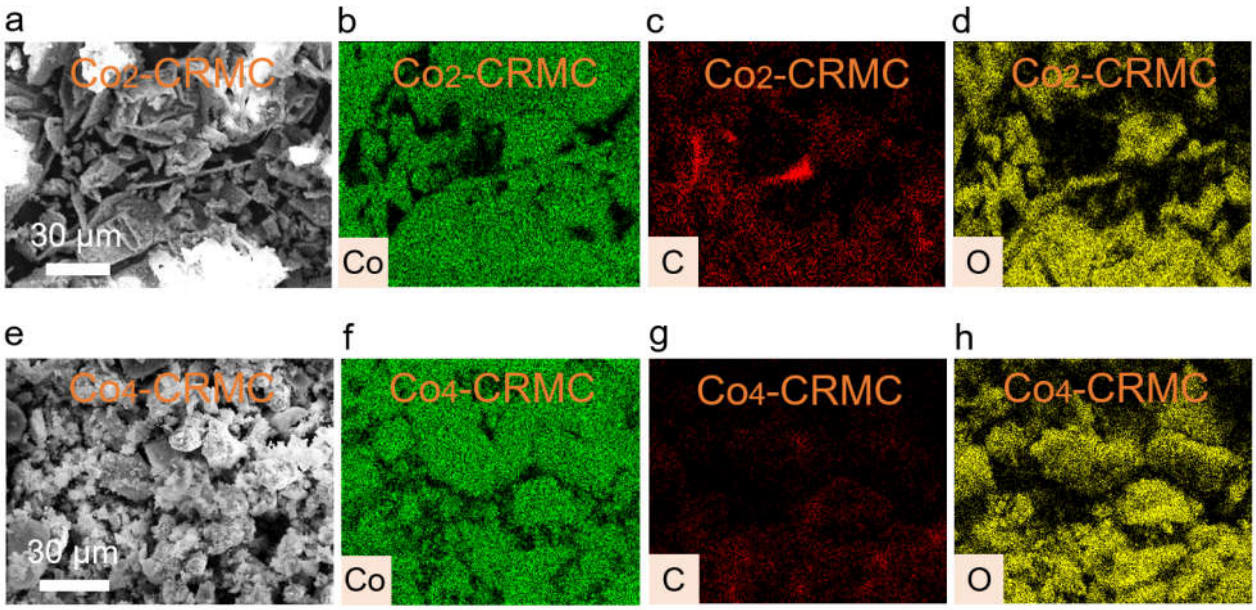

Figure S1. (a–h) SEM and corresponding elemental mapping images of (a–d) Co_2-CRMC and (e–h) Co_4-CRMC clusters, respectively.

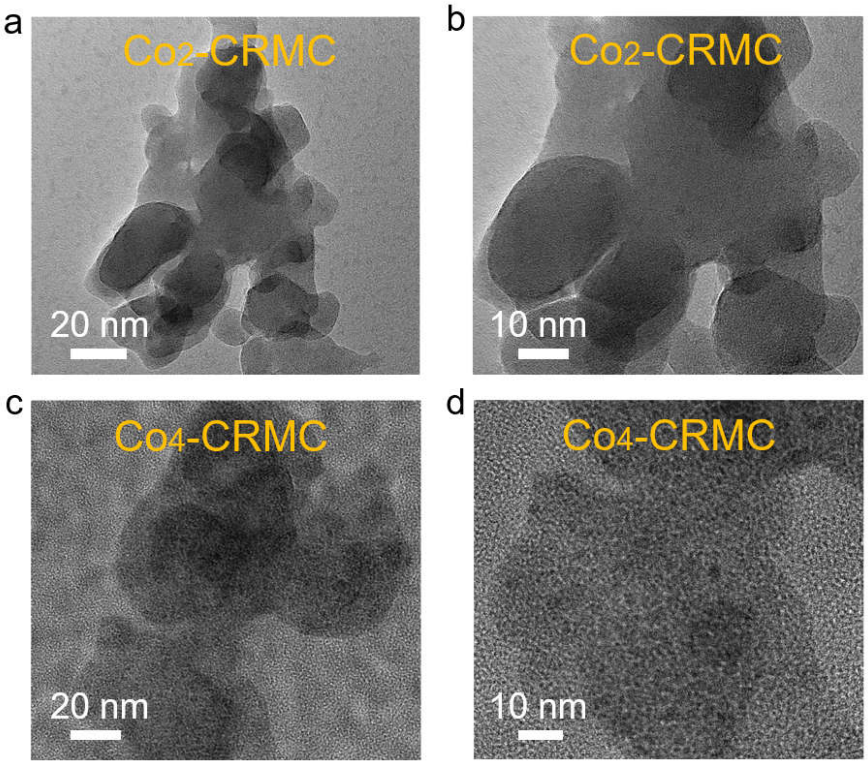

Figure S2. (a,c) Low-resolution and (b,d) high-resolution TEM images of (a,b) Co_2-CRMC and (c,d) Co_4-CRMC clusters, respectively.

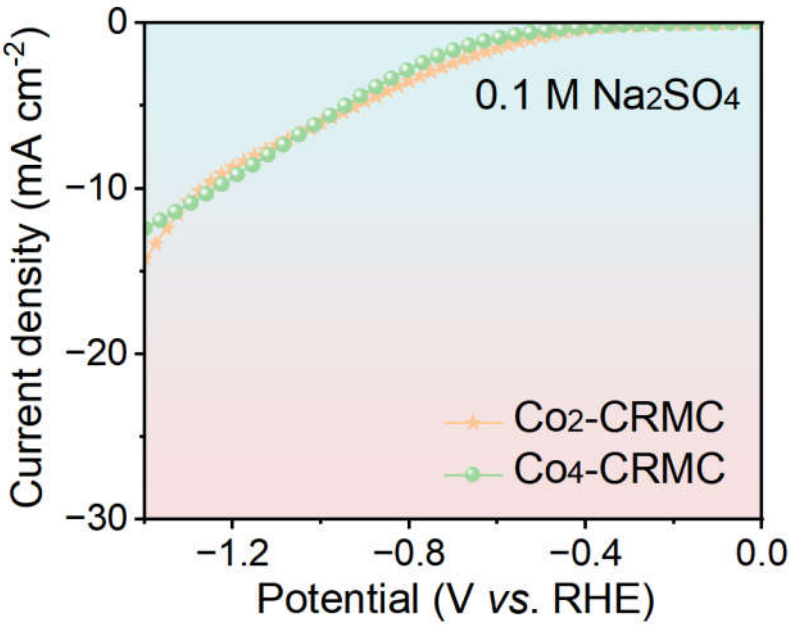

Figure S3. LSV curves of Co_2-CRMC and Co_4-CRMC electrodes tested in 0.1 M Na_2SO_4 solution without nitrate ions.

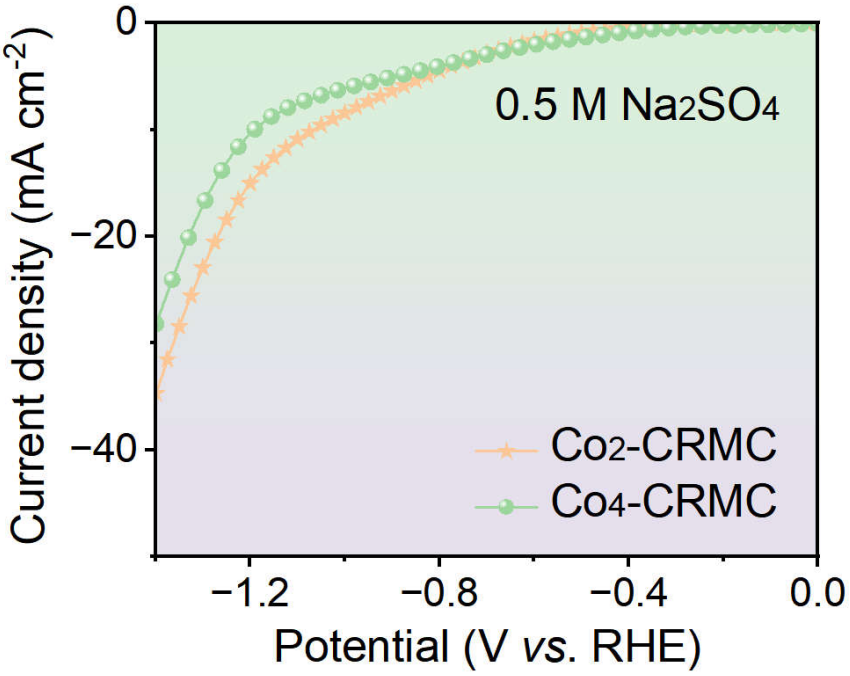

Figure S4. LSV curves of Co_2-CRMC and Co_4-CRMC electrodes tested in 0.5 M Na_2SO_4 solution without nitrate ions.

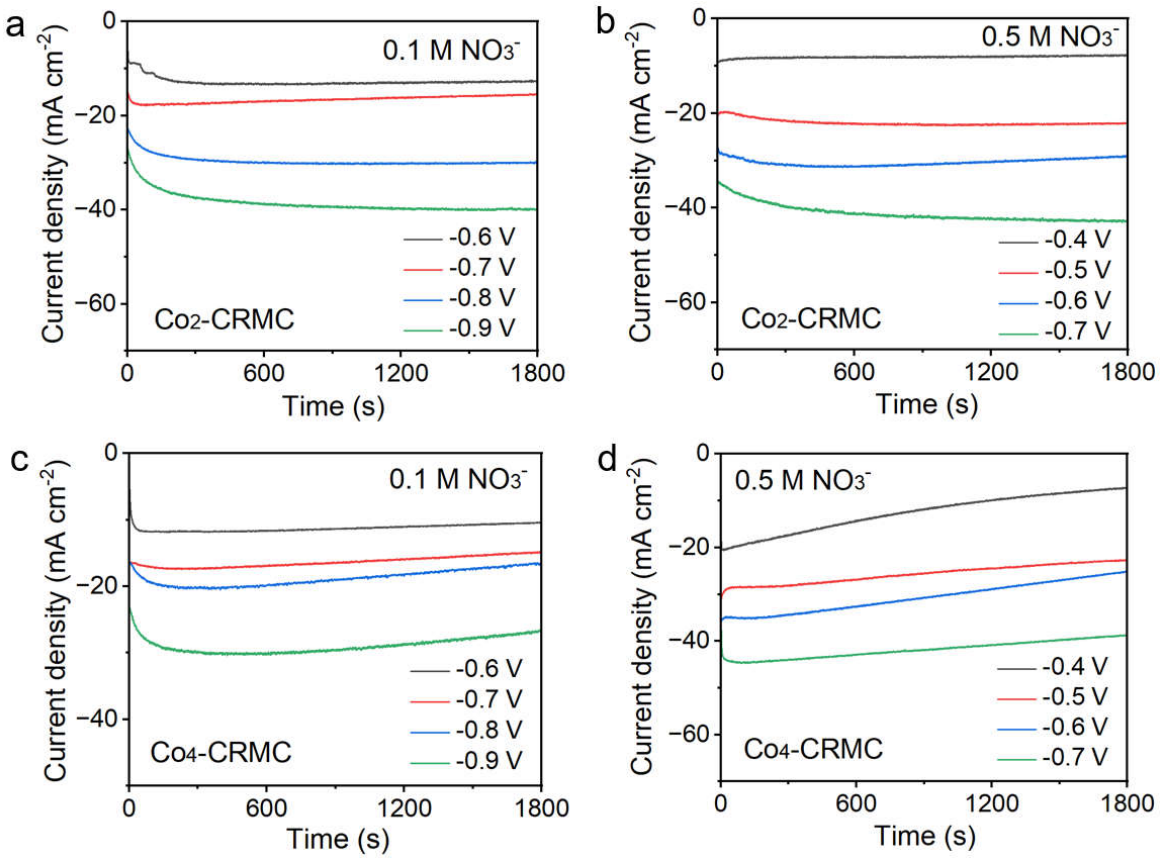

Figure S5. (a,b) Time-dependent current density curves of Co_2-CRMC electrode tested in (a) 0.1 M Na_2SO_4–0.1 M KNO_3 mixed electrolyte and (b) 0.5 M KNO_3 electrolyte, respectively. (c,d) Time-dependent current density curves of Co_4-CRMC electrode tested in (c) 0.1 M Na_2SO_4–0.1 M KNO_3 mixed electrolyte and (d) 0.5 M KNO_3 electrolyte, respectively.

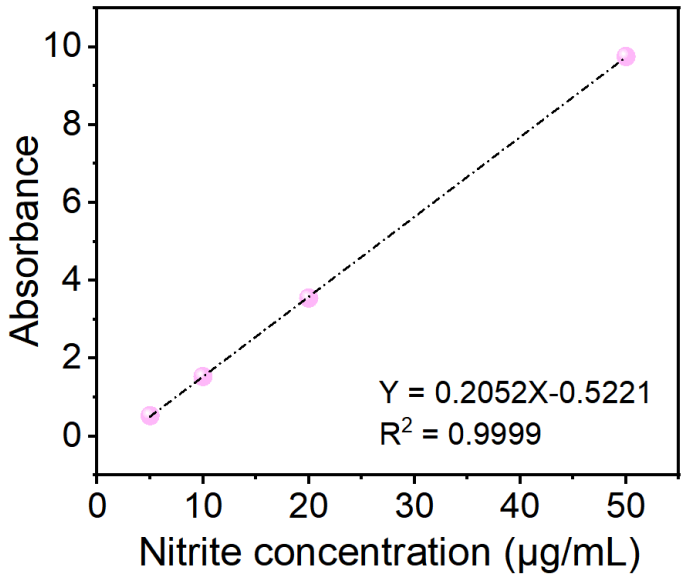

Figure S6. (a) Linear relationship of the light absorbance at 540 nm wavelength measured by UV-Vis spectrophotometer under various concentrations of $NaNO_2$ standard solutions.

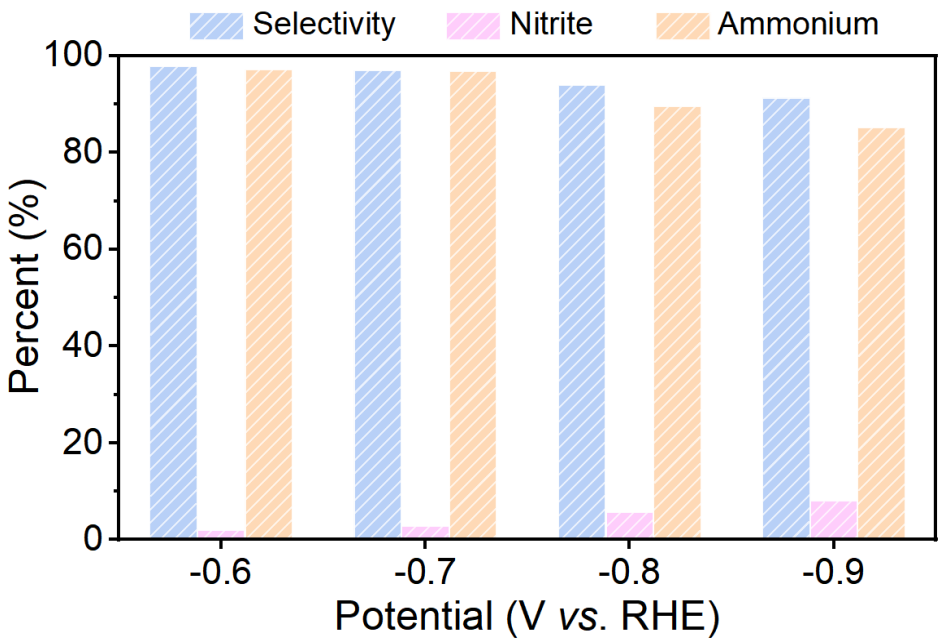

Figure S7. The FE values for the nitrogenous NH_3 and NO_2^- products, and the selectivity towards NH_3 under various applied potentials of Co_2-CRMC electrode tested in 0.1 M Na_2SO_4 solution containing 0.1 M KNO_3.

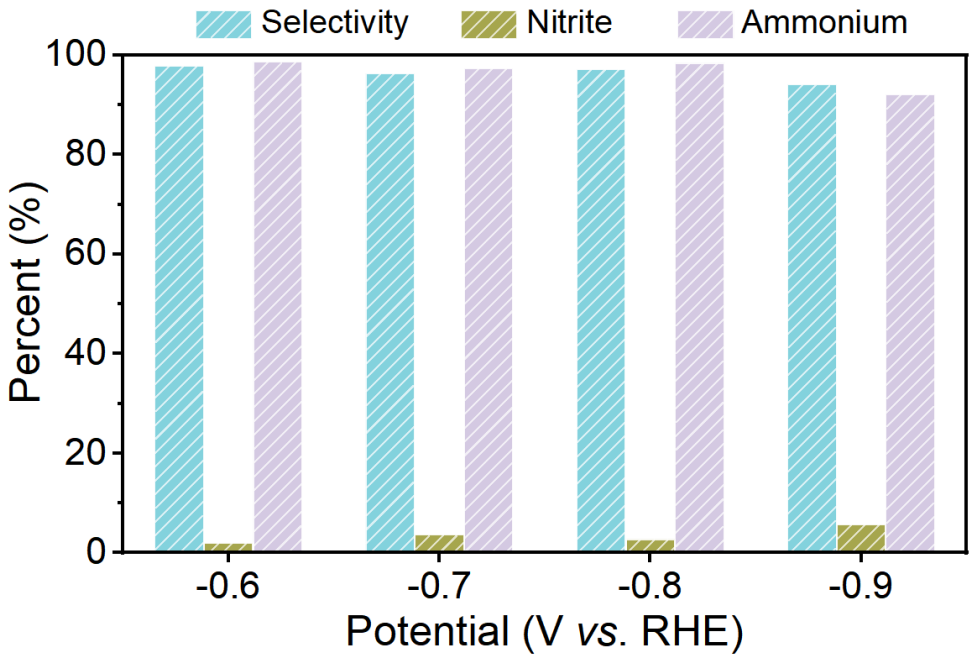

Figure S8. The FE values for the nitrogenous NH_3 and NO_2^- products, and the selectivity towards NH_3 under various applied potentials of Co_4-CRMC electrode tested in 0.1 M Na_2SO_4 solution containing 0.1 M KNO_3.

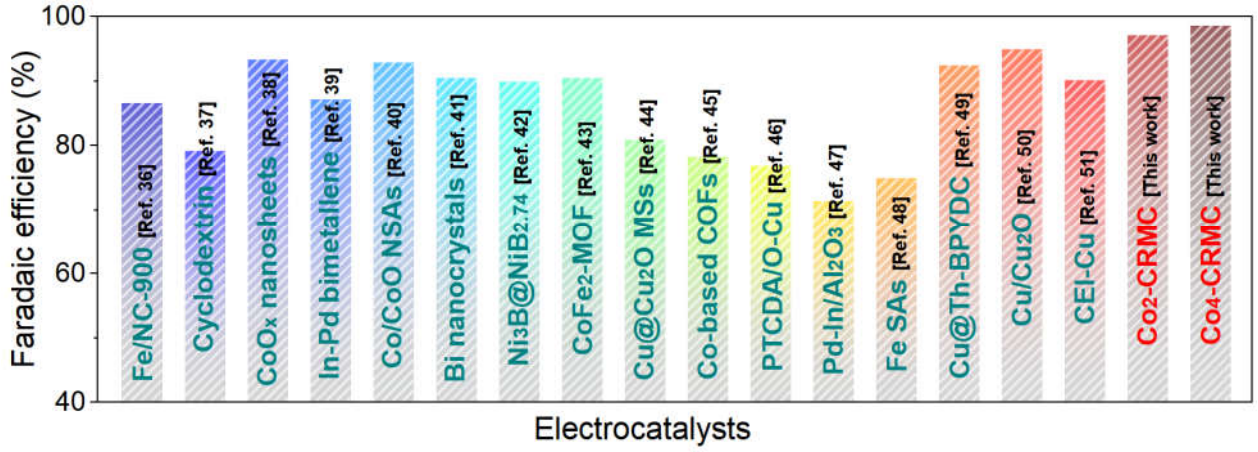

Figure S9. Electrochemical performance comparison on the FE_{NH3} values of Co_2-CRMC and Co_4-CRMC samples with other electrocatalysts reported in previous literatures.

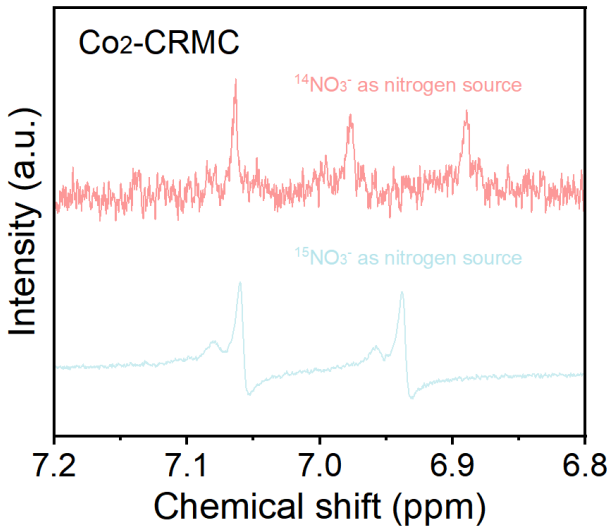

Figure S10. ^{1}H-NMR spectra of the products after the NITRR test of Co_2-CRMC electrode using $K^{14}NO_3$ and ^{15}N isotope labeled $Na^{15}NO_3$ as the feeding nitrogen sources, respectively.

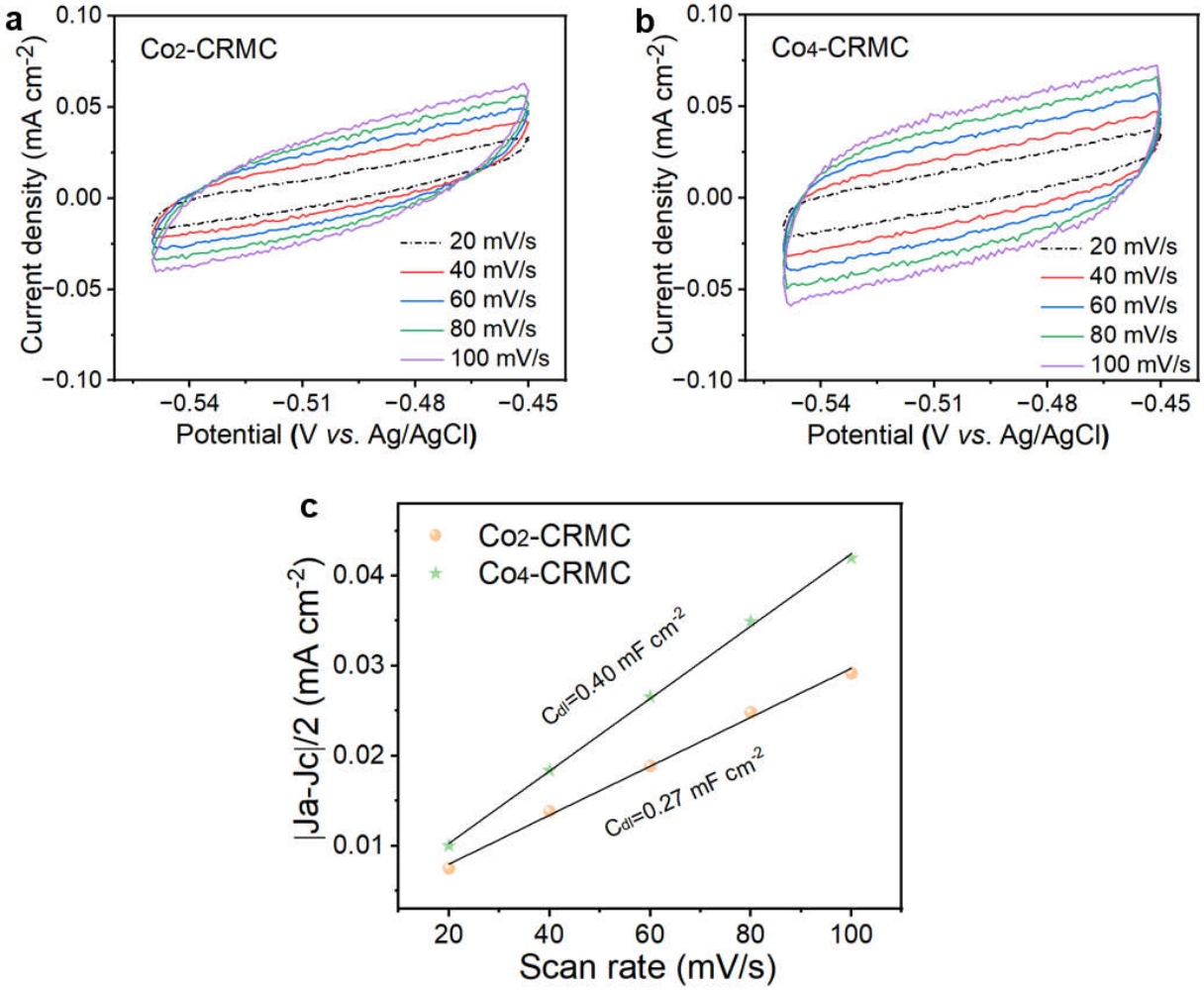

Figure S11. CV curves of (a) Co_2-CRMC and (b) Co_4-CRMC electrodes measured in 0.1 M Na_2SO_4 aqueous electrolyte, respectively. (c) The fitted plots show the extraction of the double-layer capacitance of electrodes.

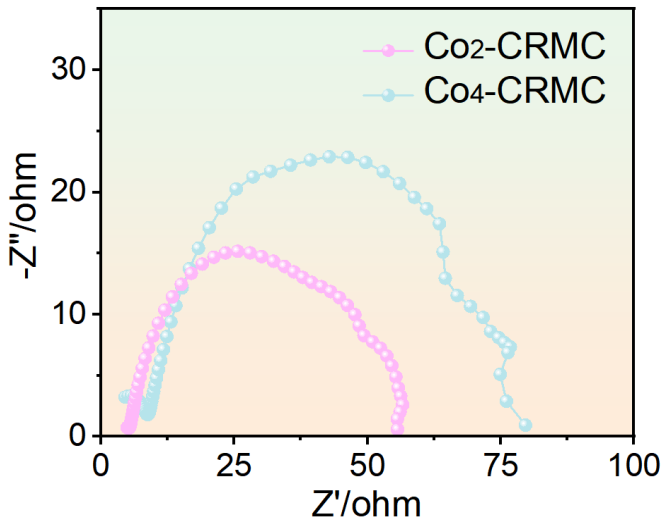

Figure S12. Nyquist plots of Co_2-CRMC and Co_4-CRMC electrodes obtained by EIS measurements.

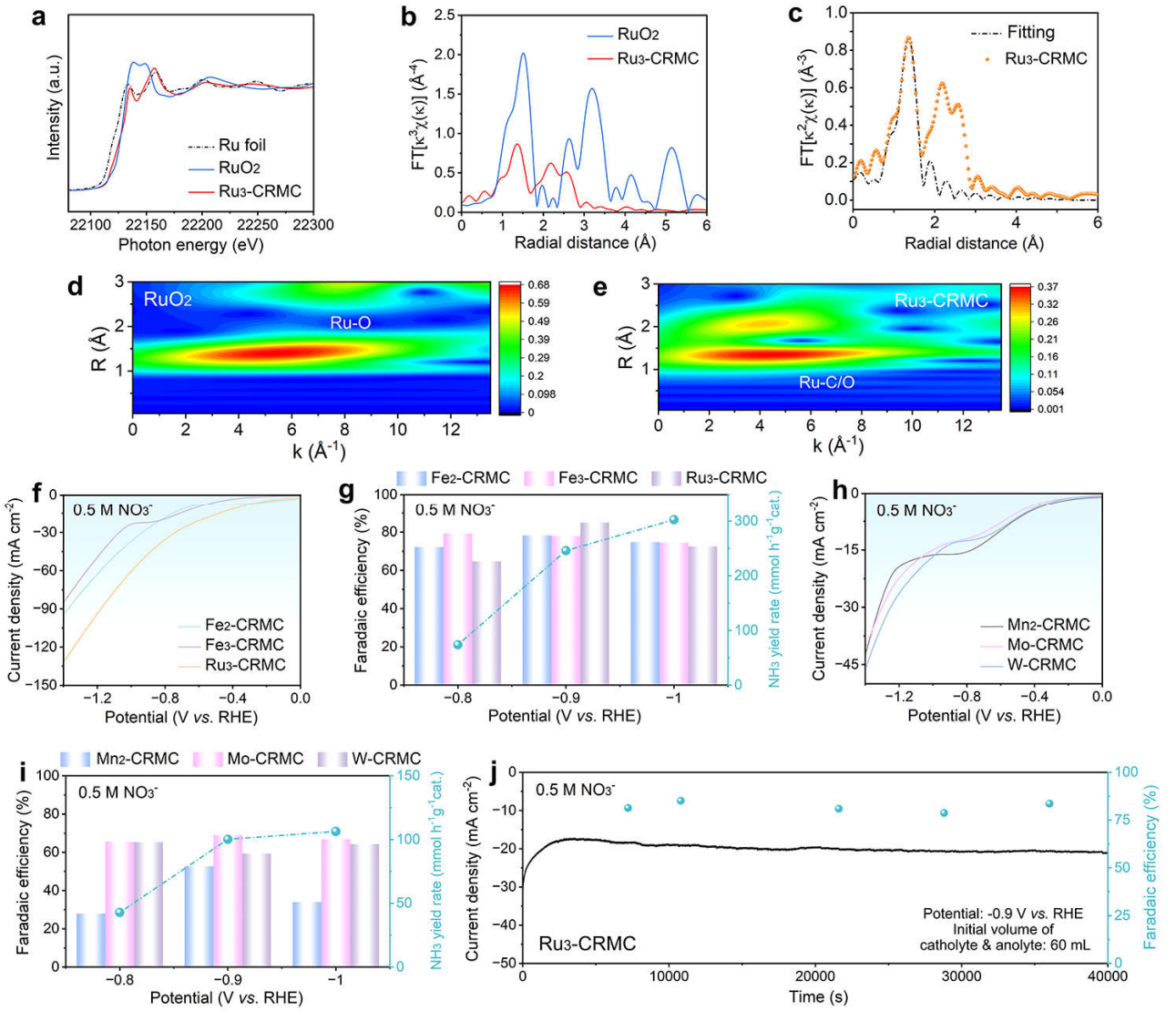

Figure S13. Fine structure characterizations and electrocatalytic NITRR tests of other carbonyl-rich metal clusters. (a) Ru K-edge XANES and (b) EXAFS spectra of carbonyl-rich Ru_3-CRMC along with other reference cluster samples. (c) The Ru K-edge EXAFS fitting curves of Ru_3-CRMC sample. (d,e) Ru K-edge wavelet transformation of Ru_3-CRMC along with the reference cluster sample. (f,h) LSV curves of various carbonyl-rich cluster electrodes tested in 0.5 M KNO_3 aqueous electrolyte. (g,i) Corresponding FE_{NH3} values and NH_3 yield rates of the carbonyl-rich cluster electrodes for the NITRR tested in 0.5 M KNO_3 electrolyte at various applied potentials. (j) Time-dependent current densities and FE values of Ru_3-CRMC cluster electrode during long-term stability test.

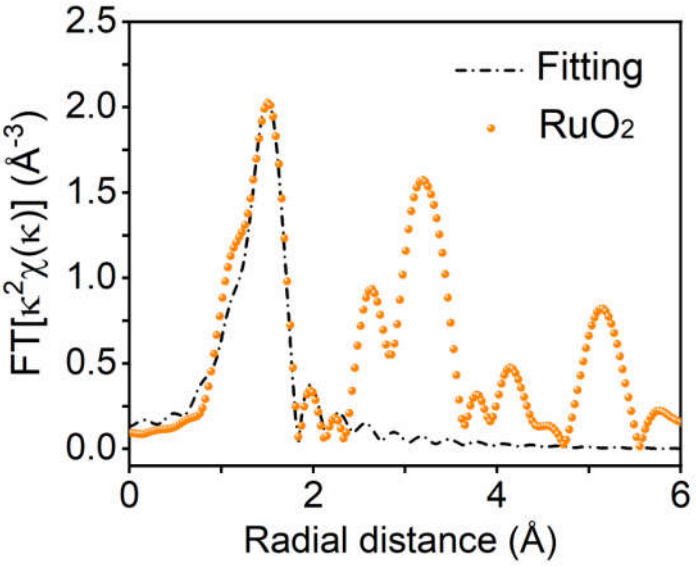

Figure S14. The Ru K-edge EXAFS fitting curve of RuO_2 sample.

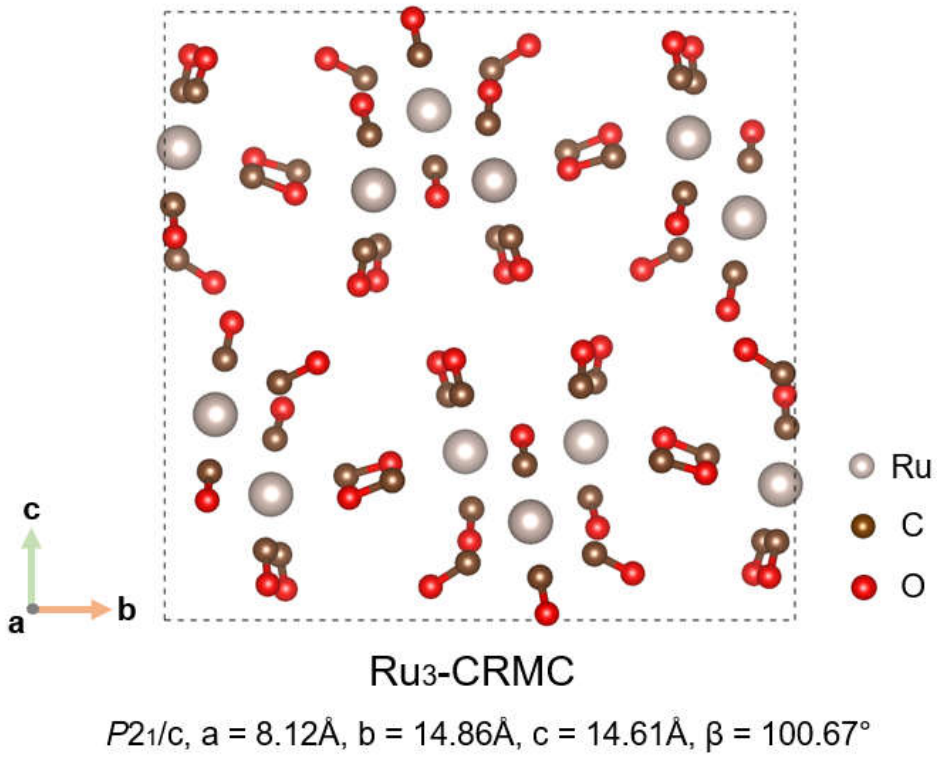

Figure S15. Crystal structure of carbonyl-rich Ru_3-CRMC cluster.

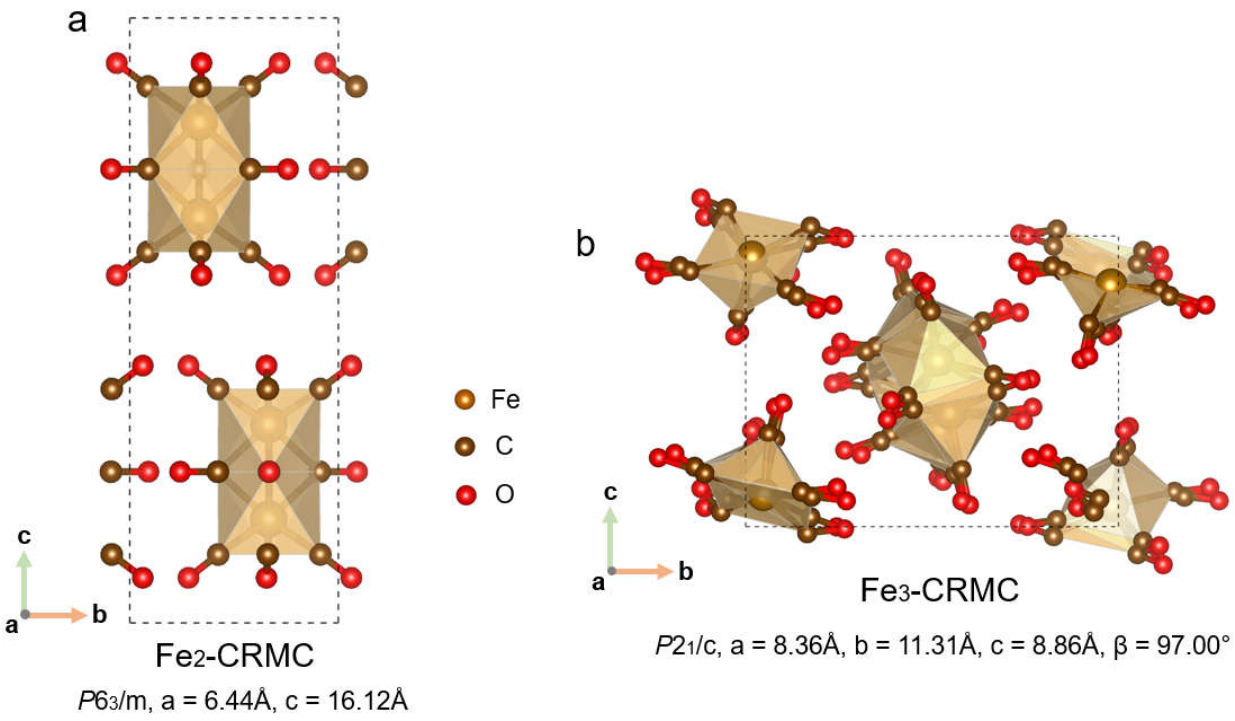

Figure S16. Crystal structures of carbonyl-rich (a) Fe_2-CRMC and (b) Fe_3-CRMC clusters, respectively.

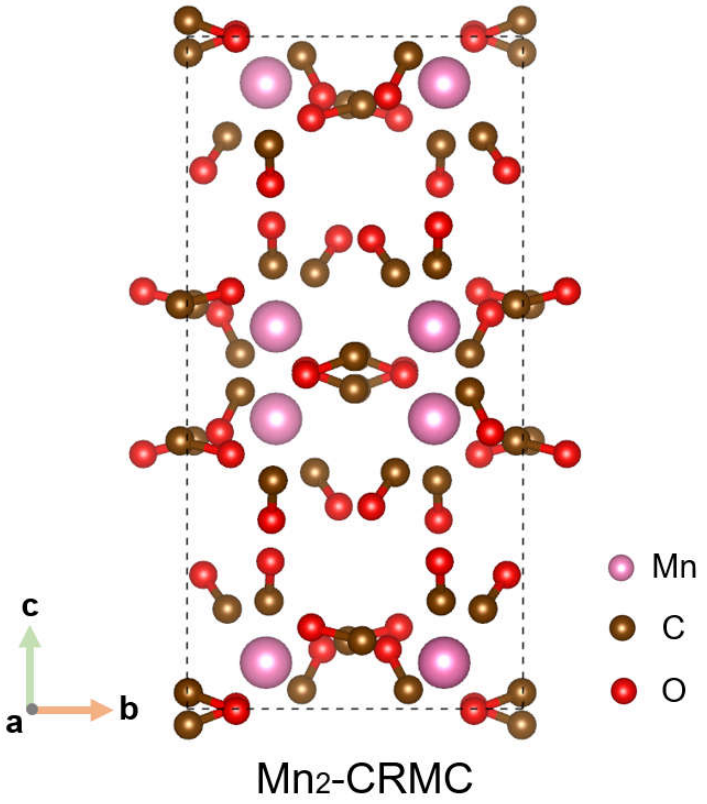

Figure S17. Crystal structure of carbonyl-rich Mn_2-CRMC cluster.

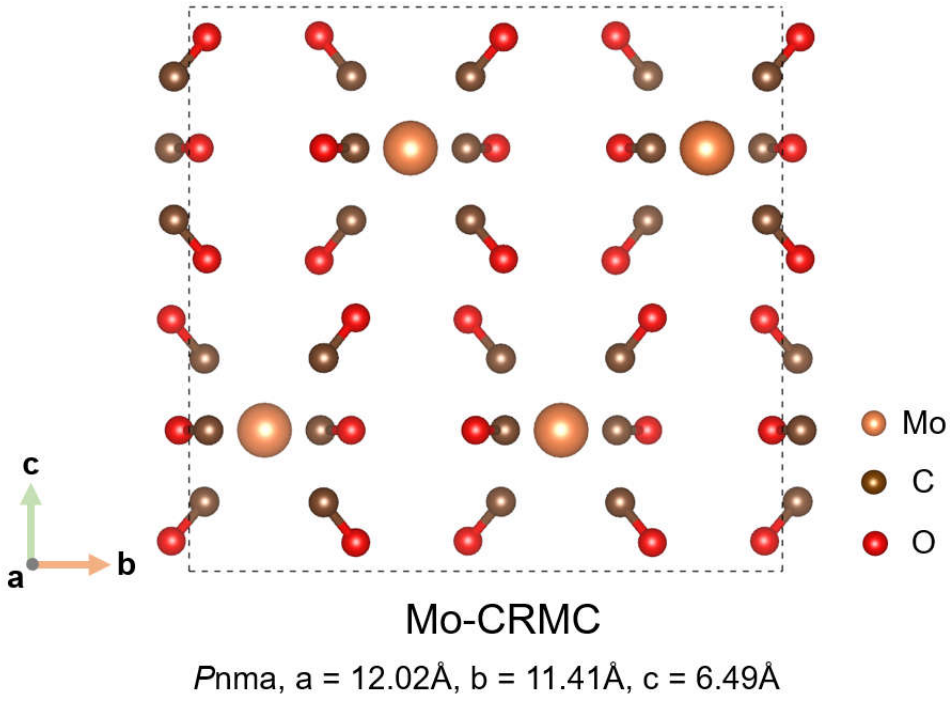

Figure S18. Crystal structure of carbonyl-rich Mo-CRMC cluster.

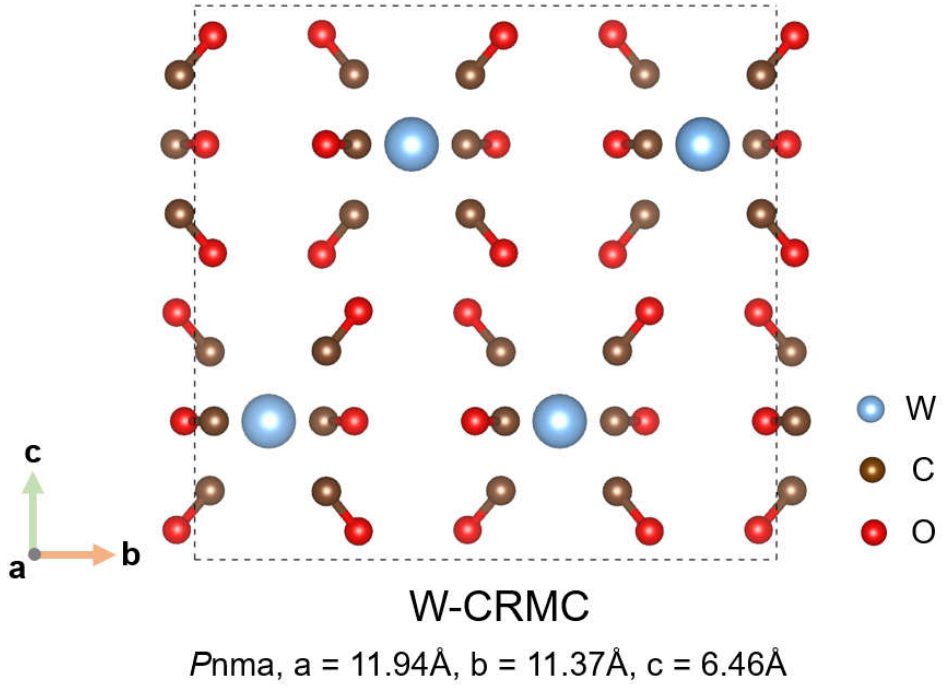

Figure S19. Crystal structure of carbonyl-rich W-CRMC cluster.

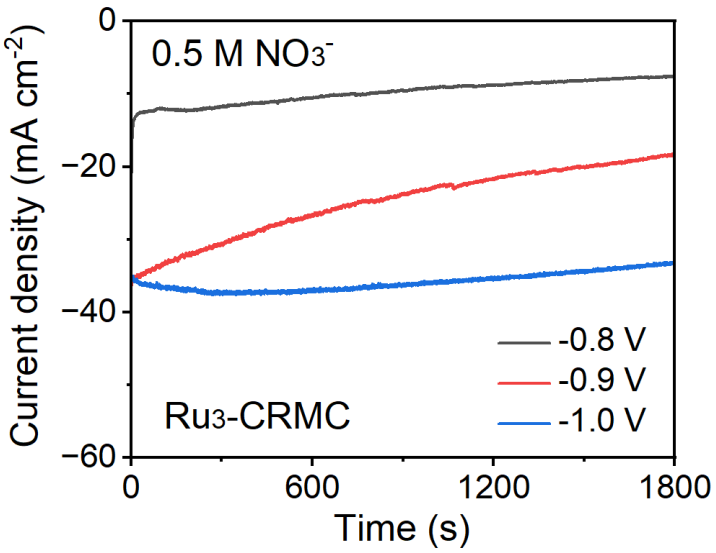

Figure S20. Time-dependent current density curves of Ru_3-CRMC electrode tested in 0.5 M KNO_3 electrolyte at various applied potentials.

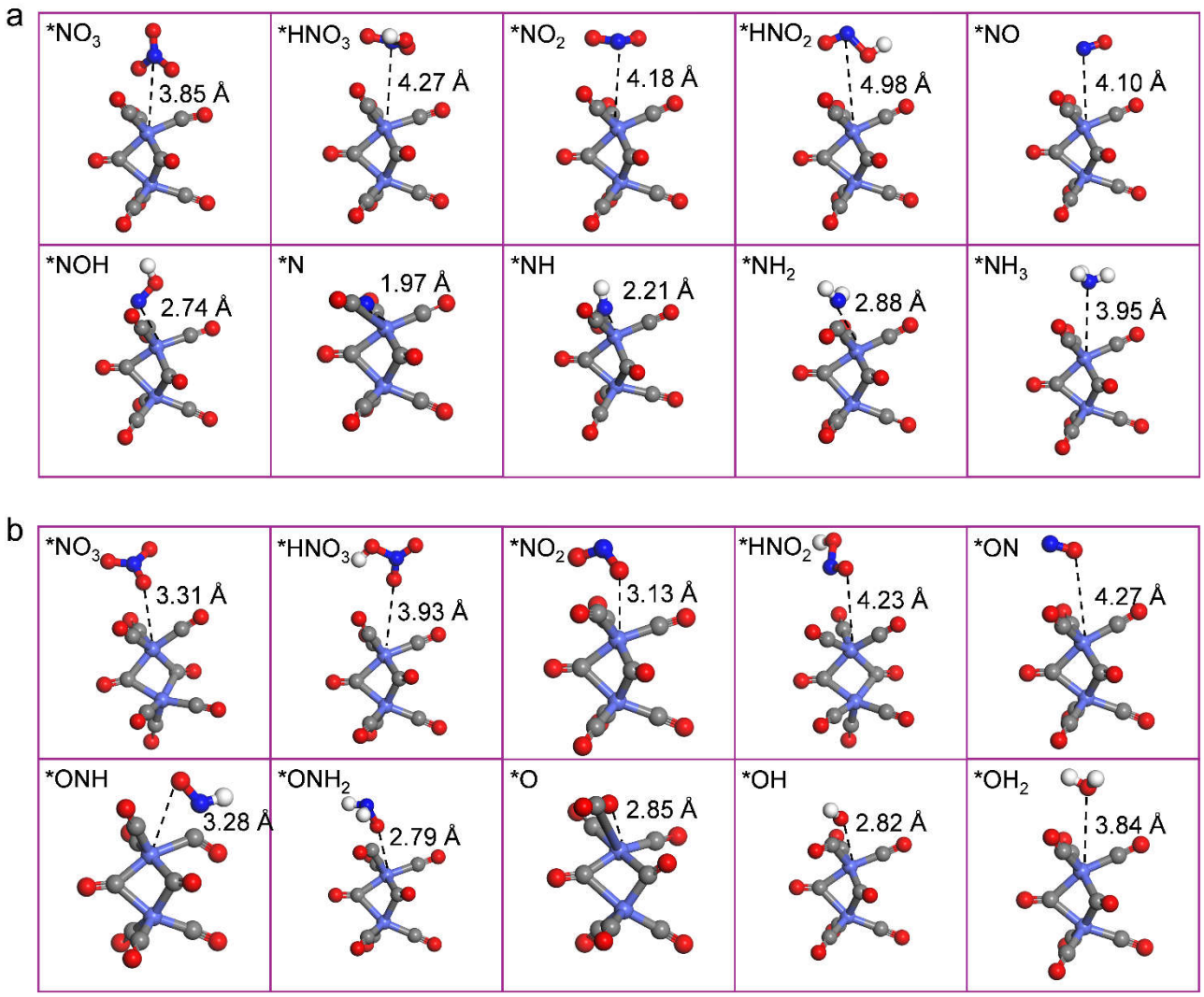

Figure S21. Optimized geometric structures of various reaction intermediates during the NITRR process on the Co_2-CRMC cluster model following the N-end and O-end pathways.

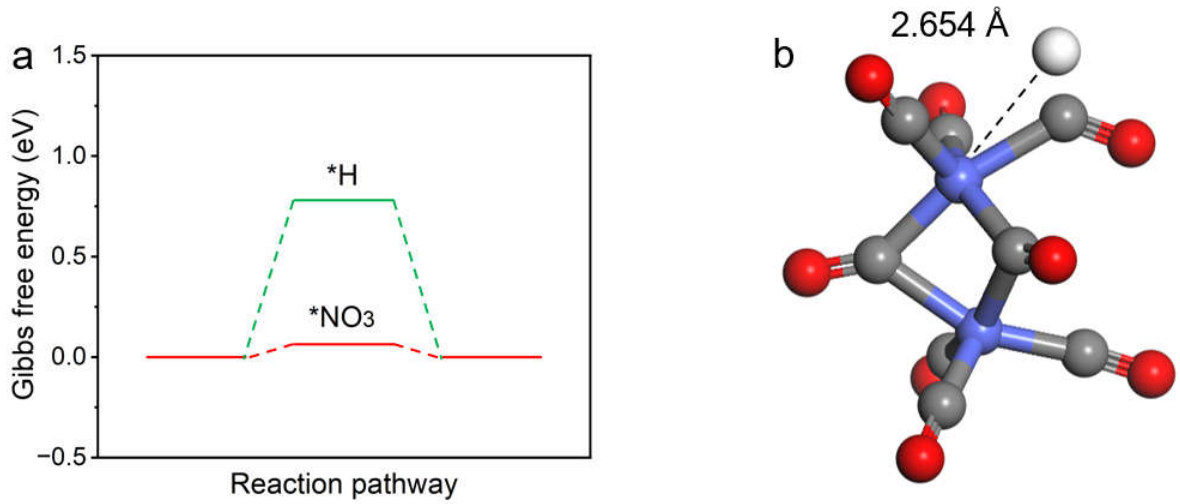

Figure S22. (a) Free energy diagram of competing electrochemical NITRR and HER processes on the Co_2-CRMC cluster model. (b) Optimized geometric structures of *H intermediate.

Table S1. Quantitative analyses of the coordination environments for Co_2-CRMC and Co_4-CRMC clusters using EXAFS fitting.

Sample	R-factor[#1]	Path[#2]	CN[#3]	R[Å][#4]	$\sigma^2[10^{-3}Å^2]$[#5]
Co foil	0.0018	Co-Co	12.0	2.49	6.1
Co_2-CRMC	0.0134	Co-C/O	4.9	2.05	8.9
		Co-C/O-O	5.0	3.35	6.1
Co_4-CRMC	0.0176	Co-C/O	3.6	2.04	4.6
		Co-C/O-O	3.6	3.41	3.2

Notes: $S_0^2 = 0.795$; [#1] Degree of curve coincidence; [#2] Scattering paths; [#3] Coordination number; [#4] Bond length; [#5] Debye-Waller factor.

Table S2. Quantitative analyses of the coordination environments for Ru_3-CRMC cluster using EXAFS fitting.

Sample	R-factor[#1]	Path[#2]	CN[#3]	R[Å][#4]	$\sigma^2[10^{-3}Å^2]$[#5]
Ru_3-CRMC	0.0158	Ru-C/O	3.9	1.87	3.1
RuO_2	0.0184	Ru-O	2	2.02	1.4
		Ru-O	4	1.95	1.7

Notes: S_0^2=0.83; [#1] Degree of curve coincidence; [#2] Scattering paths; [#3] Coordination number; [#4] Bond length; [#5] Debye-Waller factor.

Supporting References

[S1] J. P. Perdew, K. Burke, M. Ernzerhof, *Phys. Rev. Lett.*, **1996**, 77, 3865.

[S2] S. Grimme, J. Antony, S. Ehrlich, H. Krieg, *J. Chem. Phys.*, **2010**, 132, 154104.

[S3] S. Grimme, S. Ehrlich, L. Goerigk, *J. Comput. Chem.*, **2011**, 32, 1456–1465.

[S4] S. Guo, K. Heck, S. Kasiraju, H. Qian, Z. Zhao, L. C. Grabow, J. T. Miller, M. S. Wong, *ACS Catal.*, **2018**, 8, 503–515.

[S5] F. Calle-Vallejo, M. Huang, J. B. Henry, M. T. M. Koper, A. S. Bandarenka, *ACS Catal.*, **2017**, 7, 4359–4364.

[S6] D. R. Lide, *CRC Handbook of Chemistry and Physics*, 95th ed.; CRC Press: Boca Raton, FL, **2015**.